Two-dimensional-like superconducting properties and weak antilocalization transport in $FeSe_{0.4}Te_{0.6}$ single crystals: Topology-driven magnetotransport

Chin-Wei Lin [1,*] I Nan Chen [2,*] Zhujialei Lei [1] and Li Min Wang [1,†]

[1] Department of Physics/Graduate Institute of Applied Physics, National Taiwan University, Taipei 10617, Taiwan
[2] Instrumentation Center, National Taiwan University, Taipei 106, Taiwan

(Received 31 July 2023; revised 25 October 2023; accepted 21 November 2023; published 6 December 2023)

Investigations of the superconducting properties of $FeSe_{0.4}Te_{0.6}$ single crystals have demonstrated that these iron-based superconductors hold the potential to host Dirac-cone-type surface states and two-dimensional (2D) topological superconducting states. Experimental observations detected Berezinsky-Kosterlitz-Thouless transition and transport vortex dynamics, suggesting a dominant role of topological surface states in magnetotransport at low temperatures. In the normal state, $FeSe_{0.4}Te_{0.6}$ demonstrated a weak antilocalization transport feature due to the topological nature at temperatures $T < 16.5$ K and negative magnetoresistance characteristic due to the suppression of spin-disorder scattering induced by the Kondo effect as the temperature reached 40 K. Additionally, the annealing process of $FeSe_{0.4}Te_{0.6}$ single crystals caused a shift from the initial three-dimensional transport pattern to one that more closely resembles a 2D transport system. These findings support the notion that $FeSe_{0.4}Te_{0.6}$ holds promise as a platform for investigating topological superconductivity.

DOI: 10.1103/PhysRevB.108.214509

I. INTRODUCTION

Authors of studies on superconducting $FeSe_{0.5}Te_{0.5}$ and $FeSe_{0.45}Te_{0.55}$ have shown that iron-based superconductors can host Dirac-cone type surface states at the Fermi level as well as two-dimensional (2D) topological superconducting states on the surface [1–10], providing a possible high-temperature platform for realizing topological superconductivity and Majorana bound states. Thus, ion-based superconducting FeSeTe compounds have recently been revealed as leading candidate materials for 2D topological superconductivity and are important role in the development strategy of topological quantum computing [7–9]. Commonly, the topological superconductivity of $FeSe_{0.5}Te_{0.5}$ or $FeSe_{0.45}Te_{0.55}$ has been examined by angle-resolved photoelectron spectroscopy and scanning tunneling spectroscopic measurements, in which a linear-dispersion surface band state or a zero-bias conductance peak can be observed [3–9]. So far, only a few attempts have been made at exposing the topological properties of the ion-based superconducting FeSeTe families via the magnetotransport measurements, even though several studies on the transport properties of FeSeTe superconductors have been reported, as seen in review articles [11–13]. Magnetotransport properties provide an opportunity for a more fundamental understanding of electronic properties, especially for 2D materials with strong topological effects. 2D superconductivity is usually at the interfaces of heterostructures, such as $LaAlO_3/SrTiO_3$ and $Bi_2Te_3/FeTe$ heterostructures [14–18], superconducting ultrathin films [19–21], intercalated layered superconductors [22–24], and some single-crystalline thin flakes [25,26]. Intrinsic 2D superconductivity has been found only on the bulk single crystals of $AuSn_4$ [27], $Ba(Fe_{0.914}Co_{0.086})_2As_2$ [28], and highly anisotropic cuprate superconductors [29]. Recently, the discovery of the so-called topological superconductors or Weyl superconductors has stimulated strong interest in the nontrivial 2D properties due to the surface topological effect [30–32]. Through the proximate effect, 2D surface superconductivity is affected by the bulk superconductivity, resulting in nontrivial topological superconductivity (*p*-wave or spin-triplet superconductivity) as expected [33–35]. In addition, the $FeSe_{1-x}Te_x$ (FST) system exhibits intricate behaviors when changing the composition x and the annealing effects. This includes a nonlinear relationship between x and superconducting transition temperature T_c [36,37], a decrease in the upper critical field H_{c2} as x increases [38], variation in x and a dimensionality transition of vortex dynamics [38], and the impact of excess Fe impurity on flux pinning in the annealed samples [13]. Thus, it is worth conducting a more thorough examination of the magnetotransport properties of FeSeTe compounds.

In this paper, we demonstrate the 2D superconductivity nature of ∼10-μm-thick annealed $FeSe_{0.4}Te_{0.6}$ single crystals, in which a Berezinsky-Kosterlitz-Thouless (BKT) transition as well as the transport vortex dynamics interpreted in a 2D system are presented. The third critical field H_{c3} was measured to evaluate 2D surface superconductivity in $FeSe_{0.4}Te_{0.6}$. Additionally, we made a discovery: The normal-state $FeSe_{0.4}Te_{0.6}$ exhibits weak antilocalization (WAL) transport at temperatures ∼16.5 K, which could be attributed to the magnetotransports dominated by topological surface states in $FeSe_{0.4}Te_{0.6}$ single crystals at low temperatures. A rise in temperature demonstrates negative magnetoresistance (MR), possibly resulting from the reduction of spin-disorder scattering induced by Kondo effect at

*These authors contributed equally to this work.
†Corresponding author: liminwang@ntu.edu.tw

elevated temperatures. Additionally, the observed variation in the dimensions of transport properties due to the annealing effect could be attributed to the competition between spin-singlet and spin-triplet pairings induced by Fe impurities in $FeSe_{0.4}Te_{0.6}$ single crystals. The study results demonstrate that $FeSe_{0.4}Te_{0.6}$ indeed can offer a promising platform to explore the exotic properties of topological superconductivity.

II. CRYSTAL GROWTH, CHARACTERIZATION, AND EXPERIMENTAL METHODS

Single crystals of $FeSe_{0.4}Te_{0.6}$ were grown by the self-flux method using starting materials of Fe, Se, and Te powders. Appropriate amounts of high-purity elements were mixed with an alcohol solution and sealed in an evacuated quartz tube. To synthesize the single crystals, the tube was first heated up to 600 °C for 20 h to carry out preliminary chemical reactions. The obtained sample was reground, sealed in an evacuated quartz tube, and heated again at 1050 °C for 36 h. Crystal growth occurred via slow cooling at a rate of −5 °C/h from 1050 to 460 °C. From the resulting ingot, as-grown single-crystalline samples with a typical size of $2\times2\,\mathrm{mm}^2$ with $<10\,\mu\mathrm{m}$ thickness were mechanically cleaved off. The obtained crystals could be easily cleaved perpendicular to the *c* axis. Superconductivity of as-grown $FeSe_xTe_{1-x}$ single crystals can be improved by annealing with optimum conditions [36,39]. Thus, for the thermal postannealing process, the samples were resealed in an evacuated quartz tube and heated up to 400 °C at $5\,^\circ\mathrm{C\,min}^{-1}$ and kept at that temperature for 2 h. Here, the studied $FeSe_{0.4}Te_{0.6}$ single crystals are denoted as S_{asg} and S_{ann}, representing as-grown and annealed samples, respectively. The phase purity and the crystal structure of obtained crystals were characterized by powder x-ray diffraction (Bruker D2 phaser) measurement using Cu-$K\alpha$ radiation on single crystals. For the measurement of electrical transport, thin plates of cleaved $FeSe_{0.4}Te_{0.6}$ crystals were cut into dimensions of $\sim1.5\times0.5\times0.01\,\mathrm{mm}^3$. Five leads were soldered with indium, and a Hall-measurement geometry was formed for simultaneous measurements of both longitudinal (ρ_{xx}) and transverse (Hall) resistivities (ρ_{xy}) using the standard DC four-probe technique applying a DC current density of $\sim100\,\mathrm{Å/cm}^2$. The DC magnetization was measured in a superconducting quantum interference device system (MPMS from Quantum Design). Figure 1(a) shows the x-ray θ-2θ diffraction spectra for as-grown (S_{asg}) and annealed (S_{ann}) $FeSe_{0.4}Te_{0.6}$ single-crystalline specimens. As shown, diffraction peaks appeared only at (00*n*) ($n=1$, 2, 3, and 4), indicating that the *c*-axis [001] direction is perpendicular to the plane of the crystals, and the perpendicular cleaved plane to the *c* axis. The inset of Fig. 1(a) shows the x-ray θ-2θ diffraction spectra in the region near the (004) peak for the S_{asg} and S_{ann} samples. The broadening peaks exhibited a shoulder at a higher 2θ angle due to the Cu-$K\alpha_1$ and Cu-$K\alpha_2$ radiations, and the (004) peak of the S_{ann} positions is at a higher angle due to a decrease in the length of the *c* axis. The *c*-axis lattice constant was precisely determined to be 6.051 and 6.048 Å for S_{asg} and S_{ann}, respectively, which are very close to 6.050 Å, as reported in an earlier study [40]. Figure 1(b) illustrates a typical quantitative energy-dispersive x-ray spectroscopy elemental analysis on a portion of the scanning electron microscopy (SEM) image of S_{asg}, and the molecular formulas of summed Fe, Se, and Te were calculated to be $Fe_{1.03}Se_{0.39}Te_{0.61}$, close to $Fe_1Se_{0.4}Te_{0.6}$ as expected. The SEM images for samples also show a homogeneous distribution for Fe, Se, and Te elements. The inset of Fig. 1(b) is a photo of the S_{asg} sample, showing a platelike shape with a flat surface of a crystalline *ab* plane. Figure 1(c) shows the temperature-dependent magnetic susceptibility $4\pi\chi$ in zero-field-cooled (ZFC) and field-cooled (FC) modes with an applied field $H=5$ Oe for the S_{asg} and S_{ann} samples. The inset of Fig. 1(c) shows the transition at temperatures near T_c, and the transition temperature T_c is determined by an intersection of two linear fitting lines extrapolated from the normal-state and transition regions, respectively. The observed superconducting transition temperatures T_c are ∼14.03 and 14.10 K for the S_{asg} and S_{ann} samples, respectively. One can see that annealing led to a slight increase in T_c for the as-grown sample after annealing, as reported in early studies [36,39]. Using the expression [41] of $\chi=\chi_{exp}/(1-N\chi_{exp})$, the superconducting volume fraction was estimated to be ∼100% based on the magnetization at 2 K, where *N* represents the demagnetization factor according to the sample geometry and χ_{exp} is the susceptibility calculated from the original experimental data. Compared with the

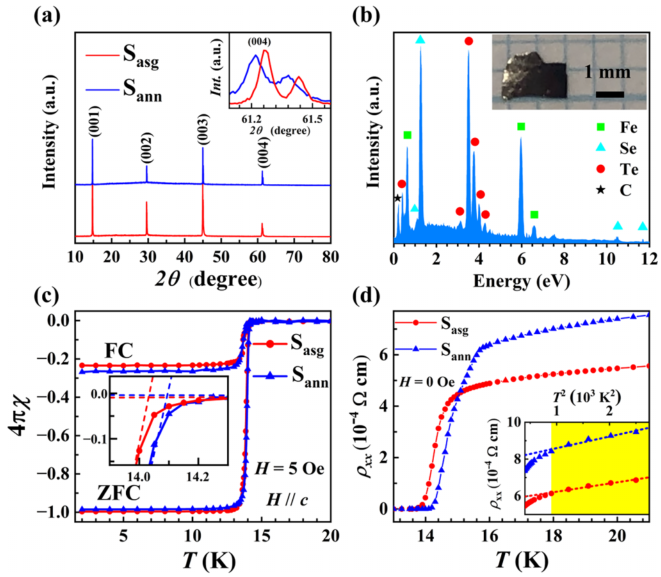

FIG. 1. Characterization of the as-grown S_{asg} and annealed S_{ann} $FeSe_{0.4}Te_{0.6}$ samples. (a) The x-ray diffraction spectrum shows the crystal structures of S_{asg} and S_{ann}. (b) The energy-dispersive x-ray spectroscopy analysis provides compositional information for both S_{asg} and S_{ann}. An unexpected peak, corresponding to carbon (C), could potentially be attributed to the environmental background. (c) Zero-field-cooled (ZFC) and field-cooled (FC) magnetizations in $H=5$ Oe parallel to the *c* axis for S_{asg} and S_{ann}. Inset: Highlights of the transition region of the temperature-dependent susceptibility curve. The dashed lines are the linear fittings of the normal state and transition regions. (d) The zero-field resistivity curves depict the temperature-dependent electrical resistivity of S_{asg} and S_{ann}. Inset: Low-temperature normal-state resistivity data, offering an insightful temperature-correlated analysis for both S_{asg} and S_{ann} and the dashed line represents the fitting of $\rho_{xx}(T)=\rho_0+AT^2$.

ZFC signal less than T_c, the much smaller FC signal indicates a strong vortex pinning in both $FeSe_{0.4}Te_{0.6}$ single crystals, in accordance with those presented by earlier works [13,42,43]. The splitting of the FC and ZFC susceptibilities is a typical feature of type-II superconductors due to the pinning effect arising from defects or impurities, where a portion of magnetic flux is pinned within the body of the superconductor upon cooling the material in an applied field. Furthermore, the slightly larger magnitude of the diamagnetic FC signal for S_{ann} implies a reduction of Fe impurities in the annealed single crystal sample, resulting in a weaker pinning [13,39]. Figure 1(d) displays the low-temperature electrical resistivity $\rho_{xx}(T)$ for the S_{asg} and S_{ann} samples in a zero-applied magnetic field, showing a sharp resistive transition at temperatures near T_c. The estimated T_c, defined as the temperature at which the resistance of the superconductor is halfway between the resistance in its normal state and its zero-resistance state, was found to be 14.28 and 15.28 K for the S_{asg} and S_{ann} samples, respectively. These results agree with the findings from magnetization measurement, shown in Fig. 1(c). The inset of Fig. 1(d) shows the low-temperature normal-state resistivity data, which could fit in the temperature range of 16–50 K using the formula $\rho_{xx}(T) = \rho_0 + AT^2$ with a residual resistivity ρ_0 of $\sim$580 $\pm$ 7 $\mu\Omega$ cm and the electron-electron scattering coefficient $A = (4.44 \pm 0.38)\times 10^{-2}\ \mu\Omega\,\mathrm{cm\,K^{-2}}$ obtained for the S_{asg} sample. Meanwhile, the S_{ann} sample had $\rho_0 = 797 \pm 15\ \mu\Omega$ cm and $A = (6.30 \pm 0.85)\times 10^{-2}\ \mu\Omega\,\mathrm{cm\,K^{-2}}$. The obtained values of ρ_0 and A were comparable with those reported earlier for $FeSe_{0.4}Te_{0.6}$ single crystals [43,44], indicating the high quality of the obtained $FeSe_{0.4}Te_{0.6}$ single crystals.

III. RESULTS AND ANALYSIS

A. Essential bulk superconductivity of $FeSe_{0.4}Te_{0.6}$ single crystals

The DC (static) magnetic measurements determined the equilibrium value of the magnetization in a sample and revealed the essential bulk superconductivity of $FeSe_{0.4}Te_{0.6}$ single crystals. Figures 2(a) and 2(b) show the field-dependent magnetization $M(H)$ curves at various temperatures for the S_{asg} and S_{ann} samples in fields parallel to the c axis, respectively. The data allowed us to extract the $H_{c1}(T)$ from a Meissner-like linear $M(H)$ regime to a nonlinear $M(H)$ response. The lower critical field $H_{c1}(T)$ corresponds to the field at which the presence of vortices into the superconductor and provides key information regarding the magnetic penetration depth and superconducting energy gap. Tracking the $\geqslant$1% deviation of the $M(H)$ curve from the linear fitting in the even lower-field regime helped us determine the lower critical field $H_{c1}(T)$. Furthermore, the temperature dependence of the magnetic penetration depth $\lambda(T)$ can be determined from H_{c1} by using the formula $\mu_0 H_{c1} = (\Phi_0/4\pi\lambda^2)\ln\kappa$, where Φ_0 is the flux quantum and κ is the Ginzburg-Landau (GL) parameter. Meanwhile, according to the nodeless Bardeen-Cooper-Schrieffer (BCS) superconducting band gap theory [45,46], the temperature dependence of each penetration depth $\lambda^{-2}(T)$ can be expressed by

$$\lambda^{-2}(T) = \frac{\Delta(T)\tanh\left[\frac{\Delta(T)}{2k_B T}\right]}{\lambda^2(0)\Delta(0)}, \qquad (1)$$

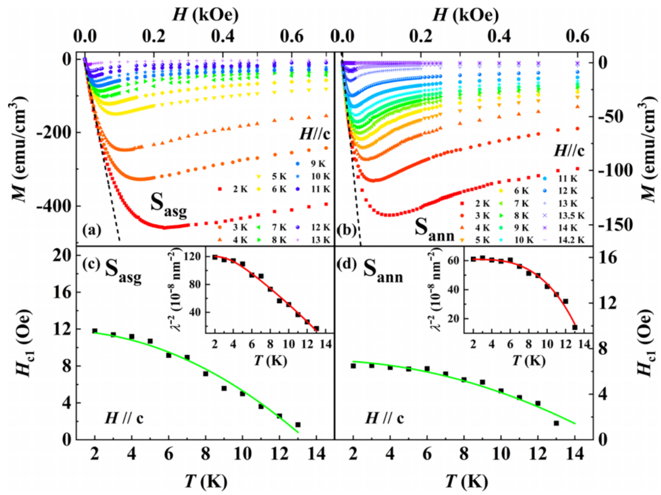

FIG. 2. Magnetic characteristics of S_{asg} and S_{ann}. (a) and (b) Out-of-plane magnetization $M(H)$ curve for S_{asg} and S_{ann} at various temperatures. The dashed line in the figure represents the linear fitting which exhibits Meissner-like behavior. (c) and (d) The temperature-dependent lower critical field derived from $M(H)$ curves for S_{asg} and S_{ann}, respectively. The green lines in the figures represent fitting curves of $H_{c1}(T)$. Insets: The penetration depth as a function of temperature derived from the lower critical field for S_{asg} and S_{ann}, respectively.

where the temperature dependence of each energy gap is $\Delta(T) = \Delta(0)\tanh[1.88(T_c/T - 1)^{0.51}]$, the Boltzmann constant k_B, each zero-temperature superconducting gap $\Delta(0)$, and the residual penetration depth $\lambda(0)$. We estimated the κ value with the ratio of penetration depth λ to coherence length ξ by considering that $\kappa = \lambda/\xi \approx (H_{c2}/H_{c1})^{1/2} = 360$ for S_{asg} and 562 for S_{ann}, where H_{c2} was determined by the resistive transition as described later, and H_{c1} was the field of the $M(H)$ curve deviating the linear behavior in the lower-field regime as mentioned previously. Figures 2(c) and 2(d) present the resulting temperature dependence H_{c1} for the S_{asg} and S_{ann} samples in fields parallel to the c axis, respectively. The data can be fitted by a function of reduced temperature $(T/T_c)^2$: $H_{c1}(T) = H_{c1}(0)[1 - (T/T_c)^2]$, illustrated by the green solid lines in Figs. 2(c) and 2(d). This alignment was consistent with the predictions of the GL equation. The insets of Figs. 2(c) and 2(d) show the temperature dependence of estimated $\lambda_{ab}^{-2}(T)$ for the S_{asg} and S_{ann} samples, respectively. As seen, the estimated $\lambda_{ab}^{-2}(T)$ could be well described using Eq. (1), indicating that the bulk superconductivity of $FeSe_{0.4}Te_{0.6}$ satisfied the traditional nodeless BCS superconducting band gap theory. The magnetization results which helped to deduce the parameters of $H_{c1}(0)$, $\lambda(0)$, and $\Delta(0)$ for the S_{asg} and S_{ann} samples are summarized in Table I. The temperature dependences of H_{c1} and λ^{-2} indicated that the bulk superconductivity of $FeSe_{0.4}Te_{0.6}$ resembles that of the s-wavelike BCS superconductor [47,48]. The values of the superconducting gap and the ratio of $2\Delta(0)/k_B T_c$ align with the findings from other studies for FeSeTe compounds [47–49].

B. 2D-like superconductivity of $FeSe_{0.4}Te_{0.6}$ revealed in the mixed-state transport

The surface superconductivity of $FeSe_{0.4}Te_{0.6}$ single crystals was explored via magnetotransport measurements for

TABLE I. Superconducting properties of S_{sag} and S_{ann}.

Parameter	Unit	S_{sag}	S_{ann}
ρ_{xx} (300 K)	Ω cm	1.22×10^{-3}	1.40×10^{-3}
T_c (magnetic)	K	14.03	14.10
T_c (electric)	K	14.28	15.25
H_{c1} (0)	Oe	11.90	6.98
$\mu_0 H_P$	T	26	28
$\mu_0 H_{c2,c}(0)$	T	51	63
$\mu_0 H_{c2,ab}(0)$	T	101	165
$\mu_0 H_{c3}(0)$	T	131	231
$\xi_c(0)$	nm	1.29	0.87
$\xi_{ab}(0)$	nm	2.53	2.28
$\lambda_{ab}(0)$	nm	911	1281
d_{sc}	nm	35.0	31.9
K	–	360	562
$\Delta(0)$	meV	1.22	2.83
$2\Delta(0)/k_B T_c$	–	2.01	4.65

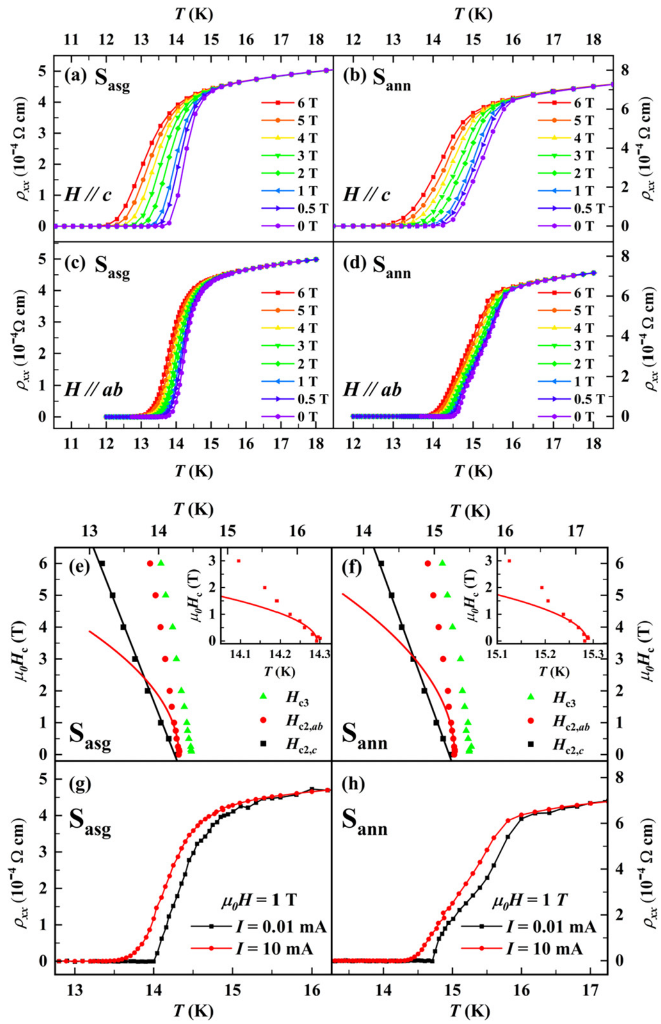

FIG. 3. Mixed-state magnetotransport in S_{asg} and S_{ann}. (a) and (b) $\rho_{xx}(T)$ curves under magnetic fields, applied perpendicularly to the sample surface plane, for S_{asg} and S_{ann}, respectively. (c) and (d) Corresponding $\rho_{xx}(T)$ curves under magnetic fields applied parallel to the sample surface for S_{asg} and S_{ann}, respectively. (e) and (f) Temperature-dependent upper critical fields $H_{c2,ab}(T)$, $H_{c2,c}(T)$, and $H_{c3}(T)$ for S_{asg} and S_{ann}, respectively. The lines represent the fitted curves of $H_{c2,c}(T) \propto (1-T/T_c)$ and $H_{c2,ab}(T) \propto (1-T/T_c)^{1/2}$. Inset: Close-up view of $H_{c2,ab}(T)$ near the critical temperature. (g) and (h) $\rho_{xx}(T)$ curves measured in a field of 1 T with 10 and 0.01 mA current, for H_{c3} estimation, for S_{asg} and S_{ann}, respectively.

samples of ∼10 μm thicknesses. Figures 3(a) and 3(b) present the resistivity as a function of temperature in magnetic fields parallel to the *c* axis for the S_{asg} and S_{ann} samples, respectively. Corresponding data of magnetic fields parallel to the *ab* plane for the S_{asg} and S_{ann} samples are shown in Figs. 3(c) and 3(d), respectively. All the resistivity curves under the magnetic field show a broadening behavior in the superconducting mixed-state region. Figures 3(e) and 3(f) present the upper critical fields in fields parallel to the *c* axis and *ab* plane (denoted by $H_{c2,c}$ and $H_{c2,ab}$, respectively) for the S_{asg} and S_{ann} samples, respectively. Here, the upper critical field H_{c2} values were derived from the 50% resistive transition. In the measured region, $H_{c2,c}(T)$ displayed a linear behavior for both S_{asg} and S_{ann} samples. On the other hand, $H_{c2,ab}(T)$ exhibited proportionality to $(1-T/T_c)^{1/2}$ only at temperatures close to T_c and within a narrow temperature region. This behavior is highlighted with a magnified view, as depicted in the insets of Figs. 3(e) and 3(f) for closer inspection. The dimensionality of superconductivity can be examined from the temperature-dependent H_{c2} [50]. For a 3D superconductor, the temperature dependences of both $H_{c2,c}(T)$ and $H_{c2,ab}(T)$ could be described as $H_{c2}(T) \propto (1-T/T_c)$, while for a 2D superconductor, the temperature dependences of $H_{c2,c}(T)$ and $H_{c2,ab}(T)$ are presented as $H_{c2,c}(T) \propto (1-T/T_c)$ and $H_{c2,ab}(T) \propto (1-T/T_c)^{1/2}$. Our observation of 2D-like H_{c2} behavior on $FeSe_{0.4}Te_{0.6}$ was like that reported for $FeSe_{0.5}Te_{0.5}$ single crystals, which presented the dependence of $H_{c2,ab}(T) \propto (1-T/T_c)^{1/2}$ at temperatures near T_c [51]. Meanwhile, the values of $H_{c2,c}(0)$ and $H_{c2,ab}(0)$ were also estimated using the Werthamar, Helfand, and Hohenberg (WHH) formula, excluding the spin-paramagnetic effect and spin-orbit interaction [52]: $H_{c2}(0) = 0.693\, T_c |dH_{c2}(T)/dT|_{T_c}$, also known as orbital-limiting field H_{orb}. Furthermore, the coherence lengths at zero temperature $\xi_{ab}(0)$ and $\xi_c(0)$ in anisotropic GL theory were related to $H_{c2,c}(0)$ and $H_{c2,ab}(0)$ according to the formulas $\xi_{ab}(0) = [\Phi_0/2\pi H_{c2,c}(0)]^{1/2}$ and $\xi_c(0) = \Phi_0/2\pi H_{c2,ab}(0)\xi_{ab}(0)$. The obtained values of zero-temperature upper critical fields $H_{c2}(0)$ and coherence lengths $\xi(0)$ for the S_{asg} and S_{ann} samples are also listed in Table I; the values are comparable with those reported in other studies [51,53]. The deduced orbital-limiting fields $H_{c2,ab}(0)$ for samples S_{asg} and S_{ann} were ∼101 and 165 T, respectively, indicating differential characteristics along the *ab* direction. In the *c* direction, the deduced $H_{c2,c}(0)$'s for S_{asg} and S_{ann} were ∼51 and 63 T, respectively, showing a higher critical field for sample S_{ann}. These estimated fields $H_{c2}(0)$ significantly overpowered the Pauli-limiting fields H_P, which were ∼26 and 28 T in this paper, with the weak coupling BCS formula $H_P \approx 1.84 T_c$. This substantial difference between the orbital- and Pauli-limiting fields suggest the presence of unconventional superconductivity. The high upper critical fields obtained for $FeSe_{0.4}Te_{0.6}$ are consistent with those reported [13,51–55] and imply that an unconventional superconductivity of perhaps triplet p-wave character in $FeSe_{0.4}Te_{0.6}$ [56].

In view of the 2D-like behavior of $H_{c2,ab}(T)$ at temperatures near T_c, we can attribute the 2D-like electrical transport to the surface conducting channel within a thickness of $\sim d_{sc}$. In Table I, we estimate the corresponding superconducting thickness d_{sc} using $H_{c2,ab}(T) = \frac{\sqrt{3}\Phi_0}{\pi \xi_{GL}(0) d_{sc}}(1-\frac{T}{T_c})^{1/2}$, based on the resulting fitting curves shown in the insets of Figs. 3(e) and 3(f). In this equation, $\xi_{GL}(0)$ represents the GL coherence length determined with the value of $\xi_{ab}(0)$. Notably, as the temperature approaches the critical temperature, the coherence length ξ_{GL} becomes larger than d_{sc}, indicating that the sample would reach the 2D superconductivity limit. Considering that $\xi_{GL}(T) = \xi_{GL}(0) \cdot (1-T/T_c)^{-1/2}$ and $\xi_{GL}(0) \approx 2.5$ nm, the crossover temperature can be estimated as $d_{sc} = \xi_{GL}$ with $d_{sc} \approx 35$ nm and a crossover temperature of $T/T_c = 0.995$ (i.e., at $T = 14.2$ and 15.2 K for S_{asg} and S_{ann}, respectively). These values align with the observed 2D behavior of $H_{c2,ab}(T)$, as shown in the insets of Figs. 3(e) and 3(f). This finding provides valuable insights into surface conductivity, which can be explored through electrical transport measurements. One way to further explore the surface superconductivity phenomenon behavior near T_c is by investigating the third critical field H_{c3}, which corresponds to a surface parallel field that the surface superconductivity can nucleate at a metal-insulator interface [57,58]. The third critical field H_{c3} is higher by a factor of 1.7 than $H_{c2,ab}$ [59–61]. Thus, the resistivity measurement with the configuration of magnetic fields parallel to the ab plane is possible to detect the contributions from both the bulk (H_{c2}) and surface (H_{c3}) superconductivity phenomena. The determination of the absolute value of H_{c3} was somewhat uncertain because the resistivity approaches the normal value in the surface sheath gradually and is affected by the measuring current. Thus, detecting H_{c3} with a very low measuring current was favorable [62]. In the transport measurement on $FeSe_{0.4}Te_{0.6}$, extremely small current densities were used for the determination of H_{c3} values. Figures 3(g) and 3(h) show the temperature dependence of resistivity by measuring current densities of 0.049 and 0.143 $\text{Å}/\text{cm}^2$ for the S_{asg} and S_{ann} samples in a surface-parallel field of 10 kOe, respectively. As seen, with a small current applied, the resistivity went to the superconducting transition at higher temperatures, corresponding to a higher critical field H_{c3} as predicted. The temperature dependence $H_{c3}(T)$ extracted from the low-current resistivity measurement for the S_{asg} and S_{ann} samples is also illustrated in Figs. 3(e) and 3(f), respectively. The zero-temperature $H_{c3}(0)$ values derived from the WHH formula for the S_{asg} and S_{ann} samples were 131 and 231 T, respectively. The data show that $H_{c3}(0) \approx 1.3 \times H_{c2,ab}(0)$ for the S_{asg} sample, whereas for the S_{ann} sample, it was $H_{c3}(0) \approx 1.4 \times H_{c2,ab}(0)$. The ratio of $H_{c3}(0)/H_{c2,ab}(0)$ for both samples is close to the theoretical value of 1.7, indicating that the magnetotransports of $FeSe_{0.4}Te_{0.6}$ single crystals were dominated by the 2D surface superconductivity in the high-field regime.

The 2D superconductivity in $FeSe_{0.4}Te_{0.6}$ was further clarified by the experiments with field angle-dependent ρ_{xx} vs H measurements at a constant temperature. Figures 4(a) and 4(b) show the magnetic field dependence of the resistivity under different angles θ at 13.8 and 14.6 K for the S_{asg} and S_{ann} samples, respectively, where θ is the tilt angle between the normal sample surface plane (parallel to the c axis) and the direction of the applied magnetic field [see the inset of Fig. 4(c)]. Clearly, the superconducting transition shifted to a higher field with the external magnetic field rotating from parallel $\theta = 0^\circ$ (H // c axis) to perpendicular $\theta = 90^\circ$ (H // surface ab plane of applied current). Figures 4(c) and 4(d) show the extracted upper critical field H_{c2} as a function of the tilted angle θ, displaying that the critical field gradually increased as the angle increased. A cusplike peak was clearly observed at $\theta = 90^\circ$ for the S_{ann} sample. The angular dependence of $H_{c2}(\theta)$ was plotted using the 2D Tinkham formula [63] $|\frac{H_{c2}(\theta)\cos\theta}{H_{c2,c}}| + [\frac{H_{c2}(\theta)\sin\theta}{H_{c2,ab}}]^2 = 1$, and the three-dimensional (3D) anisotropic GL model [64] $[\frac{H_{c2}(\theta)\cos\theta}{H_{c2,c}}]^2 + [\frac{H_{c2}(\theta)\sin\theta}{H_{c2,ab}}]^2 = 1$, using the previously obtained values of $H_{c2,c}$ ($\theta = 0^\circ$) and $H_{c2,ab}$ ($\theta = 90^\circ$). The cusp-shaped angle dependence was consistent with the 2D Tinkham formula and deviated from the 3D anisotropic GL model for the S_{ann} sample, while the S_{asg} sample exhibited a 3D-like dependence of $H_{c2}(\theta)$. The result again demonstrates that the annealed $FeSe_{0.4}Te_{0.6}$ single crystals indeed display more of the 2D nature of superconductivity.

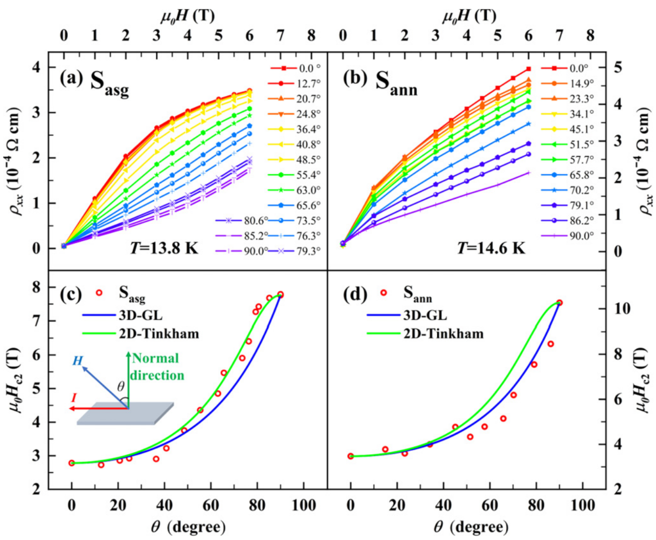

FIG. 4. (a) and (b) Variation in resistivity as a function of magnetic field at different angles θ for S_{asg} at 13.8 K and S_{ann} at 14.6 K. The angle θ is defined as the angle between the normal to the sample plane and the direction of the applied magnetic field, as illustrated in the diagram in the figure. (c) and (d) The angular dependence of the upper critical field $H_{c2}(\theta)$, obtained from the above R-H curve for S_{asg} and S_{ann}. The blue and green solid lines represent respective fits using the three-dimensional (3D) anisotropic Ginzburg-Landau (GL) and two-dimensional (2D) Tinkham formula.

The dimensionality of superconductivity can also be characterized by the mixed-state vortex dynamics under a magnetic field analyzed using thermally activated flux flow (TAFF) theory. As seen in Figs. 3(a) and 3(b), the resistivity under a magnetic field showed a broadening behavior due to thermally activated flux motion proposed by Anderson and Kim [65] and can be described by $\rho(T,H) = \rho_0 \exp(-U/k_B T)$. Here, U is the activation energy, which is normally both field and temperature dependent and corresponds

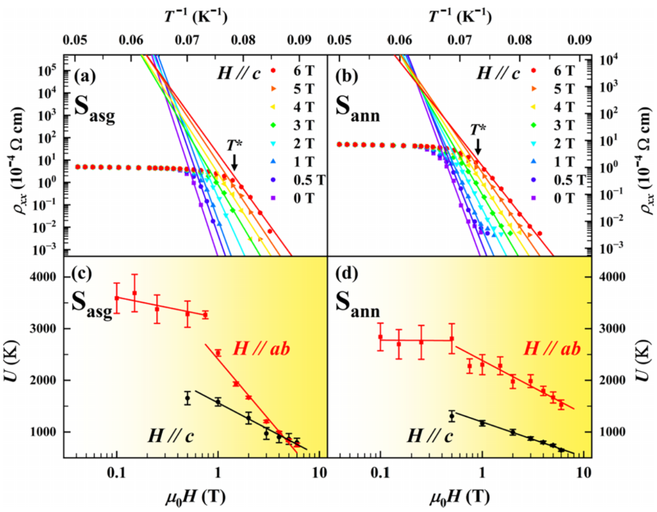

FIG. 5. (a) and (b) Arrhenius plot of resistivity in relation to magnetic fields oriented perpendicularly to the sample surface plane for S_{asg} and S_{ann}. The solid lines depict the fits of the thermally activated flux flow (TAFF) formula to the Arrhenius relationship at temperatures below T^* as indicated. (c) and (d) Magnetic-field-dependent activation energies derived from the Arrhenius plot above with magnetic fields, both perpendicular and parallel to the sample surface plane, for S_{asg} and S_{ann}. The solid lines in the figure represent the fitting of $U \propto \ln(H)$.

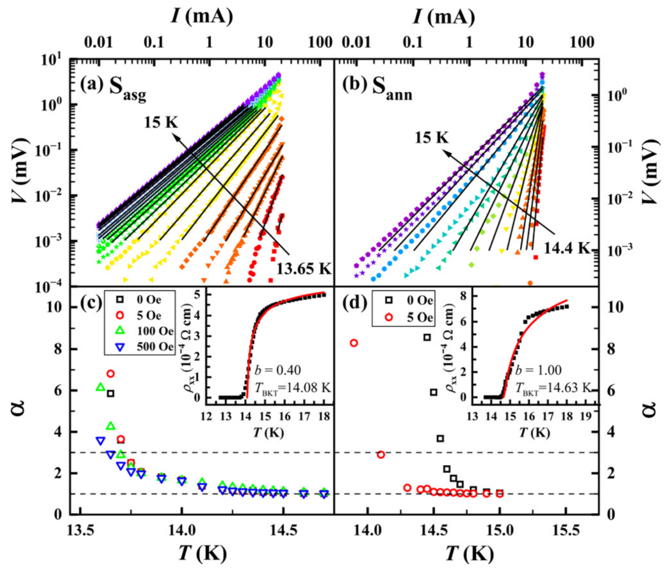

FIG. 6. Berezinsky-Kosterlitz-Thouless (BKT) nature of S_{asg} and S_{ann}. (a) and (b) *I-V* isotherms on a logarithmic scale at zero field across varying temperatures for S_{asg} and S_{ann}, respectively. Straight black lines indicate linear power-law fits to the data. (c) and (d) The temperature dependence of the power-law exponent α, derived from the power-law fits above for S_{asg} and S_{ann}. Dashed lines represent α values of 3 and 1. Inset: Highlights of the zero-field resistivity-temperature $\rho_{xx}(T)$ curve close to the BKT transition regime, corresponding with the Halperin-Nelson (HN) relation, except for the unique $\rho_{xx}(T)$ jump in the normal state, as depicted by the solid red line.

to the magnitude of effective pinning energy in the Anderson-Kim model. Figures 5(a) and 5(b) show the Arrhenius plot of resistivity as a function of $1/T$ for the S_{ann} and S_{asg} samples in the magnetic field of 1 T parallel to the crystal *c* axis and *ab* plane, respectively. The resistive transition at temperatures below a specified temperature T^* exhibited a linear behavior in the Arrhenius plot, as illustrated with straight solid lines. This indicates that the mixed-state resistivity follows the equation of thermally activated flux motion within the temperature range. Figures 5(c) and 5(d) show the field-dependent *U* extracted from the theory of Anderson and Kim [65], respectively, for the S_{ann} and S_{asg} samples, in which $U(H)$ is plotted as a function of the magnetic field on a semilogarithmic scale. The obtained *U* values for our $FeSe_{0.4}Te_{0.6}$ samples were slightly higher than those of 100–200 K for Fe(Te, Se) single crystals [66] and decreased monotonically with the increased magnetic field due to the vortex depinning arising from an increased vortex density and interaction between the vortices. Larger *U* values in the *H // ab* plane than those in the *H // c* axis demonstrate the anisotropic nature of flux pinning in layered-structure $FeSe_{0.4}Te_{0.6}$, as reported previously [67]. A relationship of $U(H) \propto -\ln(H)$ could be observed in both S_{ann} and S_{asg} samples. In the low magnetic field region under 1 T, both samples exhibited a weak dependence of *H*, which may suggest the occurrence of single-vortex pinning [68]. When the applied field *H* exceeds 1 T, a pronounced relationship between $U(H)$ and $\ln(H)$ was observed in both S_{ann} and S_{asg} samples. As pointed out, *U* was expected to follow a logarithmic dependence on the magnetic field based on the collective flux creep model in a clean 2D superconductor [69]. The 2D vortices could overcome pinning through thermal energy and demonstrate a resistance behavior, characterized by a relationship between $U(H)$ and $\ln(H)$ [70].

The observed logarithmic dependence of $U(H)$ was in accordance with the model of thermally assisted collective flux motion in 2D, as recently observed in other 2D crystalline superconductors [71–75]. Moreover, the activation energy *U* of S_{ann} was smaller than that of S_{asg} in both magnetic field directions. The observed reduction of the activation energy *U* after the annealing process is presented here. The reduced activation energy *U* indicates a decrease in the impurity levels in S_{ann} compared with S_{asg}, being in accordance with the result of FC susceptibility as discussed previously.

C. BKT transition

One way to confirm the 2D nature of superconductivity in the sample is to examine its electrical transport properties within the framework of a BKT transition, characterized by the BKT temperature T_{BKT} [76–79]. Figures 6(a) and 6(b) present the isothermal current-voltage *I-V* curves for the S_{asg} and S_{ann} samples, respectively, plotted on a logarithmic scale to reveal their power-law behavior $V \propto I^{\alpha}$. The temperature measured in Fig. 6(a) ranged from 13.6 to 15 K, with current in the range of 10 mA to 20 μA. In Fig. 6(b), the temperature measured ranged from 14.4 to 15 K, with the same current range in Fig. 6(a). When *T* exceeded T_c, the *I-V* curves exhibited a slope of 1 on the logarithmic scale, indicating ohmic behavior of the system. When the temperature was at T_{BKT}, the logarithmic *I-V* curve of the system shows a slope of 3, in line with theoretical predictions $V \propto I^3$. This specific value indicates the onset of the BKT transition.

The power-law exponent α of S_{asg} and S_{ann} extracted from Figs. 6(a) and 6(b) are presented in Figs. 6(c) and 6(d), respectively. The isothermal *I-V* curves were also examined under a small applied field, which should break up vortex-antivortex pairs and suppress the BKT transition. The behavior of BKT transition could be further verified. The BKT theory proposes a form of the Halperin-Nelson (HN) relation [80] to describe the zero-field resistivity $\rho_{xx}(T)$ for a 2D superconductor. The HN relation at temperatures just above $T_{\rm BKT}$ is expressed as $\rho_{xx}(T) = \rho_n \exp[-b(T - T_{\rm BKT})^{-0.5}]$, where ρ_n and b are material-dependent parameters.

The temperature dependences of the zero-field power-law exponent α in Fig. 6(c) decreased gradually to be 1.0 (ohmic character) for temperatures higher than $T_{\rm BKT}$, showing the characteristic of a BKT transition occurring at $T_{\rm BKT} \approx 13.74$ K in the S_{asg} sample. The inset in Fig. 6(c) shows the $\rho_{xx}(T)$ curve of the S_{asg} sample. The red line in the inset is the HN relation fitting of the zero-field $\rho_{xx}(T)$ curve above the $T_{\rm BKT}$ regime with $\rho_n = 6.24\times10^{-4}\,\Omega\,{\rm cm}$, $T_{\rm BKT} = 14.08$ K, and $b = 0.40\,{\rm K}^{1/2}$. Although $T_{\rm BKT}$ obtained from the α-T plot decreased gradually with the external magnetic fields, the α-T relation did not appear to be greatly influenced by the magnetic fields. The discernibility of the change became more pronounced with the magnetic field up to 500 Oe. This phenomenon was not consistent with the behavior of a 2D BKT transition. The S_{asg} more likely exhibited 3D transport behavior. With strong spin-orbital coupling (SOC) in an iron-chalcogenide superconductor, quantum anomalous vortices (QAVs) were formed spontaneously due to the interaction of a magnetic impurity and SOC. QAVs were 3D bulk vortices, and the presence of hysteresis in these QAVs could suggest the breaking of time-reversal symmetry. Thus, an external magnetic field could interact with the magnetic moments of the impurities, potentially altering the formation and behavior of QAVs. The observed suppression depicted in Fig. 6(c) may be attributed to the influence of a strong magnetic field on the 3D QAVs [81].

In the case of the S_{ann} sample shown in Fig. 6(d), the value of α approaches 3 at 14.57 K temperature. The display of results gradually diminished and decreased continuously from 5.9 to 1.0. The inset demonstrates that the zero-field $\rho_{xx}(T)$ curve is also well described by the HN relation with $\rho_n = 13.21\times10^{-4}\,\Omega\,{\rm cm}$, $T_{\rm BKT} = 14.63$ K, and $b = 1.00\,{\rm K}^{1/2}$. The $T_{\rm BKT}$ of the S_{ann} sample obtained from the two approaches were highly consistent and corresponded closely to T_c. Additionally, the corresponding isothermal *I-V* curves with an applied field of 5 Oe are also illustrated in Fig. 6(d). Compared with the results of zero field, a 5 Oe magnetic field can induce a significant suppression of the BKT transition in the S_{ann} sample. Here, $T_{\rm BKT}$ undergoes a substantial decrease from 14.57 to 14.10 K. The experimental results demonstrated that the S_{ann} sample, after undergoing annealing, transformed into the S_{asg} sample, exhibiting a transition from predominantly 3D transport to a nearly 2D transport.

D. Normal-state WAL transport

A negative or positive MR, due to weak localization (WL) or WAL effect, respectively, has been regarded as a signature of magnetotransport properties for topological materials [27,82–85]. The WL or WAL effect is a quantum-transport phenomena of electronic systems in a diffusive transport regime, mainly arising from the interference of a wave function in a topological surface state. WL differs from WAL based on its effects on electron movement. In WL, electrons moving in opposite directions interfere constructively, causing a decrease in resistance. However, WAL results in destructive interference, inducing electron backscattering and decreasing conductivity while increasing resistivity. When a perpendicular magnetic field is applied, it induces opposite phase shifts for counterclockwise and clockwise paths, impacting electron transport. Consequently, the measured resistance varies with the applied magnetic field [86]. The topological surface conductivity contribution due to WL can be described by $\sigma_{\rm WL} \propto \sqrt{H}$, whereas the WAL transport is described as $\sigma_{\rm WAL} \propto -\sqrt{H}$, giving a negative or positive contribution for transverse MR [87]. Thus, the conductivity contribution due to WL and WAL effects can be described by the formula:

$$\begin{aligned}\sigma &= \sigma_0 + \sigma_{\rm WL,\ WAL} + \sigma_{\rm N}\\ &= \sigma_0 \pm a(T)\sqrt{H} + (\rho_{\rm N0} + A_{\rm N}H^2)^{-1},\end{aligned} \qquad (2)$$

where σ_0 is the residual conductivity, $\sigma_{\rm WL}$ and $\sigma_{\rm WAL}$ are the topological surface conductivity from WL and WAL corrections, respectively, related to intranodal scattering, $a(T)$ is a positive temperature-dependent coefficient, and $\sigma_{\rm N}$ is the commonly considered positive MR due to the conventional nonlinear band contribution around the Fermi level and has the field dependence of $\sigma_{\rm N} = (\rho_{\rm N0} + A_{\rm N}H^2)^{-1}$ with a temperature-dependent coefficient $A_{\rm N}$ [87]. Hence, to conduct a comprehensive quantitative analysis based on Eq. (2), it is necessary to perform fitting of the magnetoconductivity, accounting for both WL and WAL effects.

Figures 7(a) and 7(b) respectively present the results of normal-state MR of the S_{asg} and S_{ann} samples, defined as ${\rm MR}(H) = [\rho_{xx}(H) - \rho_{xx}(0)]/\rho_{xx}(0)$, with applied fields perpendicular to the sample surface and temperature from 15 to 200 K. Within the magnetic field range of 6 T, positive and negative MR exhibited a monotonic behavior with respect to the magnetic field. Also, the positive MR showed a significantly greater magnitude of variation than negative MR across the entire range of magnetic fields. At low temperatures, at ∼15 K, a pronounced decrease in the resistivity of the normal state was observed. As the temperature increased, the resistivity at low magnetic fields decreased more extensively, while the MR demonstrates a linear behavior at higher magnetic fields. The dip in positive MR at lower temperatures implies the presence of the WAL effect [87]. As temperature increased, the broadening of the MR dip at small magnetic fields corresponded to a diminishing phase coherence length at these elevated temperatures. In the high magnetic field region of the positive MR, the MR exhibited a linear behavior. This behavior is likely due to the combined contribution of the bulk insulating and metallic surface states that form two parallel conduction channels. A crossover field (H*) was determined by identifying the intersection point of two linear fitting lines depicted in the figures. Above this field, the normal-state transport properties exhibit a crossover from WAL-dominated to linear-dependent-like behavior of MR. As the temperature increased, the phase coherence length

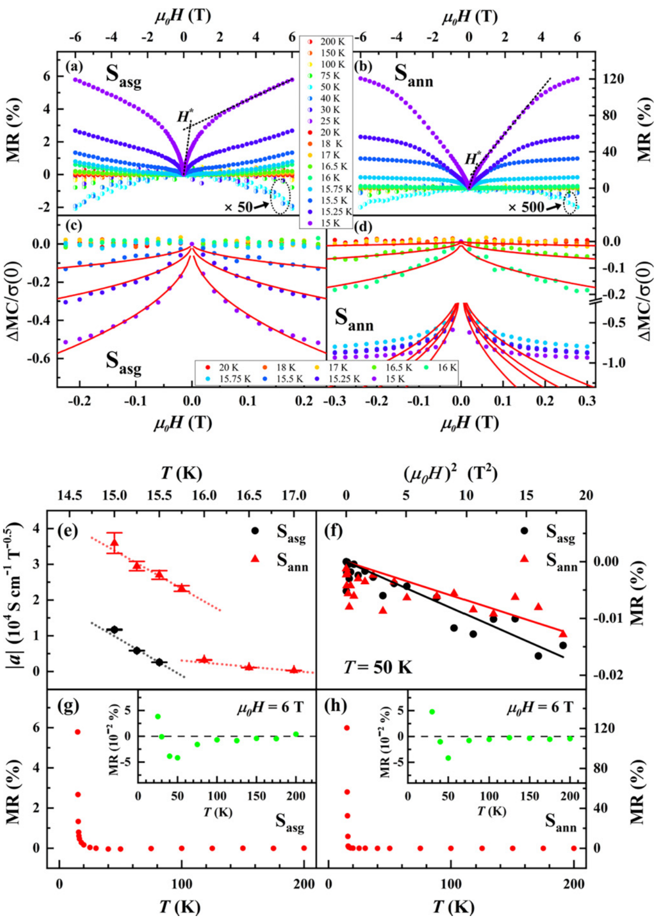

FIG. 7. Normal-state magnetoresistance (MR) and magnetoconductivity of S_{asg} and S_{ann} samples. (a) and (b) Field-dependent normal-state MR with applied fields perpendicular to the sample surface of S_{asg} and S_{ann}, respectively. The temperature range for the measurements spans from 15 to 200 K. To improve clarity, the negative MR values of S_{asg} and S_{ann} are multiplied by factors of 50 and 500, respectively. The intersection of two dashed lines denotes the crossover field H^*. (c) and (d) The transverse magnetoconductivity change ratio $\Delta MC/\sigma(0)$ with temperature in the range of 15–20 K. The red lines in both figures represent the fittings of the weak antilocalization (WAL) formula. (e) Corresponding temperature dependences of WAL parameters $a(T)$ of S_{asg} and S_{ann}, respectively. A gradual decrease within the WAL effects as the temperature increases indicates their gradual absence. The dotted lines serve the purpose of guiding the eye. (f) The MR in relation to H^2 for both S_{asg} and S_{ann}. The depicted solid line highlights a linear correlation, indicating the Kondo effect. (g) and (h) The temperature-dependent MR at magnetic field of 6 T for S_{asg} and S_{ann} samples. Insets: A magnified view of the MR near zero, highlighting the occurrence of negative extremum around 50 K for both samples.

decreased, and the dominance of the bulk states over the surface state contribution became more prominent [88]. For the S_{asg} sample, the MR exhibited a tiny negative value at $T > 30$ K. As the temperature increased, the absolute magnitude of the variation of MR with respect to the magnetic field progressively increased, reaching a maximum of ∼50 K. Moreover, as the temperature further increased, the variation of MR with respect to the magnetic field decreased gradually. The behavior of the MR in the S_{ann} sample was parallel to that of the S_{asg} sample. The MR underwent a sign change from positive to negative when the temperature reached 40 K. Subsequently, the absolute variation of the negative MR relative to the magnetic field also reached its maximum ∼50 K. While the MR behavior in both samples was comparable, the MR variation in the S_{ann} sample was noticeably greater than that in the S_{asg} sample.

Figures 7(c) and 7(d) display the change ratio in magnetoconductivity $\Delta MC/\sigma(0)$, defined as $\Delta MC = \sigma(H) - \sigma(0)$ with respect to the applied magnetic field for S_{asg} and S_{ann}, respectively. As mentioned above, the MR/ΔMC data can present strong evidence of topological surface states, signified by the observed WAL effect. The WAL effect is a product of strong SOC within the band structure, leading to a distinctive phenomenon known as spin-momentum locking in the topological surface states. Consequently, this effect becomes a common occurrence in topological materials, acting as a key manifestation of this spin-momentum locking. Additionally, the complete suppression of backscattering, a hallmark of surface states, further corroborates the presence of WAL and emphasizes its role as a critical indicator of topological surface states. The field dependence of the magnetoconductivity change ΔMC fits with Eq. (2) mentioned above, represented as the red line in the figure. The WAL transport formula aligns closely with the magnetoconductivity change ΔMC with the negligible contribution of normal conductivity (σ_N) at low temperatures. This implies a dominance of topological surface states induced by strong SOC and demonstrated by the characteristic WAL effect. The corresponding temperature dependence of the fitting parameter $a(T)$ for the S_{asg} and S_{ann} samples is illustrated in Fig. 7(e). The observed decrease in $|a|$ values with respect to increasing temperature indicates a gradual absence of the WAL effect on the field-dependent transverse magnetoconductivity. The dotted lines in the figure are for the purpose of guiding the eye. The steep dip in MR and the sharp tip in MC seen in both S_{asg} and S_{ann} are consistent with the observations reported in $AuSn_4$ [27] single crystals, Bi_2Te_3 thin films [82], and Bi_2Se_3 films deposited on nonmagnetic Al_2O_3 substrates [85], strongly suggesting the manifestation of 2D behavior from the topological surface states. Furthermore, it is worth nothing that the predicted square root behavior of ΔMC for the topological case is not well observed in the S_{ann} sample at temperatures <15.75 K. This characteristic of S_{ann} will be discussed in the following sections. In this context, the MR/ΔMC data present strong evidence for the essential magnetotransport properties of $FeSe_{0.4}Te_{0.6}$, in which the topological superconductivity was examined and signified by the observed WAL effect for the first time. This observation aligns with the previous findings in articles that relied on angle-resolved photoemission spectroscopy (ARPES), scanning tunneling microscopy (STM)/spectroscopy, and density functional theory [1–10].

As the temperature rises, the WAL effect decreases in both samples. As mentioned above, both samples exhibited negative MR at temperatures $T > 40$ K. The parabolic field dependence of negative MR may signify the potential Kondo effect on MR. The temperature-dependent changes in mobility could impact the Kondo effect and lead to

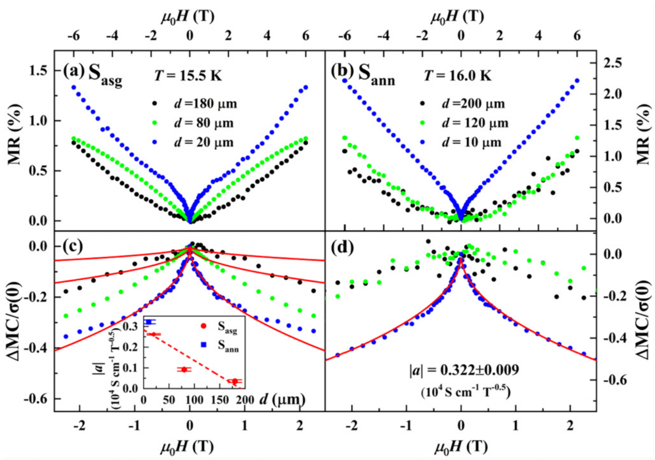

FIG. 8. (a) and (b) Illustration of normal-state magnetoresistance (MR) at 15.5 K for both as-grown and annealed $FeSe_{0.4}Te_{0.6}$ samples, each with varying thicknesses. (c) and (d) The corresponding changes in magnetoconductance [$\Delta MC/\sigma(0)$] for $FeSe_{0.4}Te_{0.6}$ samples of different thicknesses, after the comparison of both as-grown and annealed samples. Inset: The thickness dependency of the absolute values of parameter a, suggesting that the occurrence of WAL gradually decreases as sample thickness increases. The dashed line serves as a visual guide.

fluctuations in the MR. The competing balance between thermal agitation and the Kondo effect could cause negative MR. The field-dependent Kondo effect can be expressed as $MR(H) = -S(T) \cdot H^2$, where $S(T)$ represents the coefficient of MR [89,90]. Shown in Fig. 7(f) is MR as a function of the square of applied field H for samples S_{asg} and S_{ann} at 50 K. MR showed a linear dependence with the square of the field MR $\propto -H^2$, suggesting the presence of the Kondo effect [91,92]. Figures 7(g) and 7(h) show the temperature-dependent MR of the S_{asg} and S_{ann} samples with a magnetic field of 6 T. As the temperature increased, MR of both samples became negative, reaching a minimum value of $\sim -0.05\%$ at $\sim$50 K. The Kondo effect in the system could result from the interaction between charge carriers and the fluctuating magnetic moments of interstitial Fe ions. The presence of these ions may induce spin-flip scattering in the carriers, causing alterations in the MR.

WAL may signify the presence of topological surface states within a system, particularly those that exhibit strong SOC. To confirm the implications of these topological surface states, we further investigated the WAL transport behavior on samples with varying volumes. Figure 8(a) illustrates MR for the as-grown sample with thicknesses of 20, 80, and 180 μm at 15.5 K. Meanwhile, Fig. 8(b) depicts MR for the annealed sample with thicknesses of 10, 120, and 200 μm at 16 K. The field-dependent MR variations demonstrate an inverse correlation with the thickness of the samples. This is a promising observation, as thinner samples are more desirable, as they reduce the contribution from bulk conductivity. This suggests that MR behavior, being predominantly influenced by effects on topological surface electrons, is better observed in thinner samples. Figures 8(c) and 8(d) are corresponding conductance ΔMC for different thicknesses of as-grown and annealed samples, respectively. The solid lines in both figures represent the fitting curves of the WAL equation mentioned above. The WAL parameter a obtained from the fitting in relation to the sample thickness is illustrated in the inset figure. The result suggests the presence of a topological surface state in both as-grown and annealed samples. The WAL effect progressively diminishes as the thickness of the as-grown samples increases. The dashed line in the inset serves as a guide to the eye, indicating that the WAL effect decreases with an increase in sample thickness. It is noted that, for the annealed samples, only the 10-μm-thick sample can be well described by the WAL formula. For both as-grown and annealed $FeSe_{0.4}Te_{0.6}$ single crystals, the normal-state behavior just above T_c of thinner ones exhibited a more pronounced influence from the WAL effect of the topological surface state.

IV. DISCUSSION

A. H-T phase diagrams

The comprehensive conclusions of as-grown and annealed samples (S_{asg} and S_{ann}, respectively) are illustrated in phase diagrams in Figs. 9(a) and 9(b), respectively. The diagrams are constructed using the abovementioned results, including the lower critical field $H_{c1}(T)$, the characteristic temperature $T^*(H)$, the upper critical fields $H_{c2,c}(T)$ and $H_{c3}(T)$, and the normal-state characteristic field $H^*(T)$. These diagrams illustrate the transformation of transport properties in response to changes in vortex dynamics and band structure in terms of magnetic field and temperature. The S_{asg} and S_{ann} samples presented similar phase diagrams. In regions of low temperatures and low magnetic fields, the samples exhibited typical BCS superconductivity characteristics. The Meissner state (MS) of BCS bulk superconductivity is defined by $H_{c1}(T)$ and is marked as the light green region. The values of the lower critical fields were relatively small for both samples, so we multiplied them by a factor of 10^4 to highlight this region more distinctly. As the magnetic field intensified, it penetrated the sample, inducing the formation of vortices. Driven by thermal fluctuations, these vortices moved and demonstrated 2D transport characteristics. This mixed-state region (represented in blue) is known as TAFF. When the temperature and magnetic field further increased, it entered the flux flow (FF) region (represented in gray). At this point, the characteristics of the vortices were mainly affected by the applied magnetic field or electric current. We used the characteristic temperature $T^*(H)$ to distinguish between the TAFF and FF regions, as shown in Fig. 5(a). The FF region ended at the upper critical field $H_{c2,c}$, representing the disappearance of superconductivity of the type-II superconductors. Furthermore, we introduced the third critical field H_{c3} and BKT measurements to assess 2D surface superconductivity. The presence of 2D superconductivity in 200 nm $FeSe_{0.3}Te_{0.7}$ thin films has been confirmed through the BKT transition [93]. The region between $H_{c2,c}$ and H_{c3} signifies the presence of surface superconductivity, which is classified as a surface-superconductivity-dominated (SSCD) phase (illustrated in light red). The WHH curves of $H_{c2,c}(T)$ and $H_{c3}(T)$, as mentioned previously, were incorporated into the phase diagram. Above the mix-state region, we measured MR to examine its topological properties. In addition to having a larger

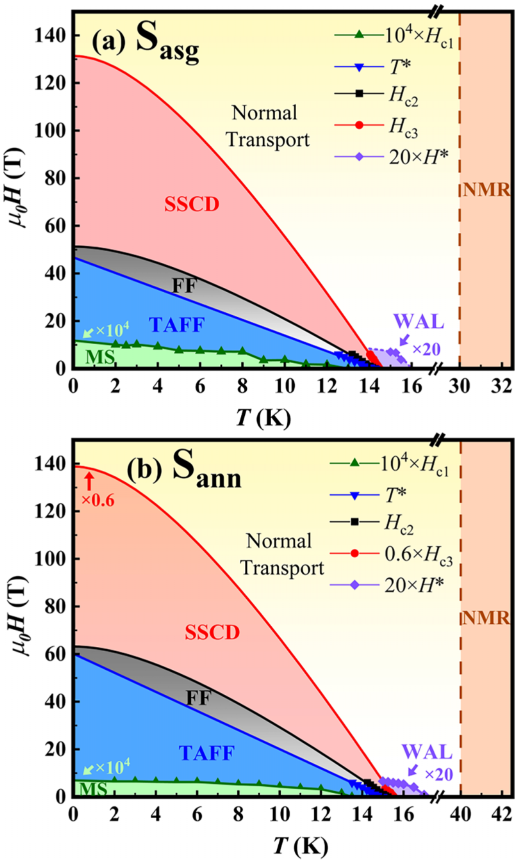

FIG. 9. (a) and (b) Phase diagrams of S_{asg} and S_{ann}, respectively, depict the variations in properties considering magnetic field and temperature. The diagrams incorporate results from $H_{c1}(T)$, $T^*(H)$, $H_{c2,c}(T)$, $H_{c3}(T)$ [$H_{c3}(T)$ for S_{ann} was multiplied by a factor of 0.6], and the normal-state $H^*(T)$. The ratio of the normal state to $H^*(T)$ (multiplied by a factor of 20) indicates a transition from weak antilocalization (WAL)-dominant transport (highlighted in cyan) to a negative magnetoresistance (MR) transport (highlighted in purple). The surface-superconductivity-dominated (SSCD) phase, separated from the normal state by the $H_{c3}(T)$ line. $H_{c2,c}(T)$ then determine the superconducting mixed state, consisting of a thermally activated flux flow (TAFF) regime (region in blue) and an flux flow (FF) regime (shaded in green), differentiated by the temperature $T^*(H)$. At sufficiently low temperatures and magnetic fields, the Meissner state (MS, shaded in green) of superconductivity is characterized by the $H_{c1}(T)$ line (multiplied by a factor of 10^4). Conversely, when the temperature is high, negative MR can be observed (region in purple).

orbital field, it also exhibited a larger spin-orbit scattering, preventing its critical field from becoming very large at low temperatures. In conditions where temperatures exceed the transition temperature, the transport properties were primarily influenced by WAL effects, depicted in cyan. The WAL effects were mainly encountered within systems with 2D structure and significant SOC. Until now, MR of various compositions $Fe_{1+y}Se_{1-x}Te_x$ has been proposed as a means to address the transition from incoherent to coherent electronic states [94]. However, in previous experiments, the samples were ∼1 mm thick, and they only observed negative MR without any WAL effects. As temperature further increased, the impact of the WAL effect diminished gradually. The system then entered a state characterized by negative MR, marked in purple. This transformation could link to the onset of the Kondo effect.

B. Differing characteristics of as-grown and annealed samples

Even though their diagrams are similar, the samples exhibited different dimension characteristics in magnetotransport properties. In sample S_{asg}, we mainly observed 3D-like electrical transportation, whereas in sample S_{ann}, 2D-like transportation was observed. This phenomenon could be related to the topological superconducting state of the $FeSe_{1-x}Te_x$ single crystals, in which zero-energy vortex-bound states have been detected within the vortex cores on the surface of samples [3,95,96], as evidenced by STM. However, both vortexes, observed with and without zero-energy states, could be attributed to the different behaviors of singlet and triplet pairing [97–101]. As indicated, under weak Zeeman coupling, typically the intraorbital singlet pairing that dominates, leading to zero-energy states being localized at the ends of the vortex on the surface. Conversely, when the Zeeman coupling due to more Fe impurities intensifies to a substantial degree, the vortices with zero-energy states delocalize and extend into the bulk of the superconductor [100]. Our findings have been explained by prior research.

The observed large orbital limiting fields in both S_{asg} and S_{ann} samples may be attributed to the spin-triplet pairing induced by the presence of Fe impurities [97]. After the annealing, the iron (Fe) impurities in the S_{ann} sample were expected to reduce [13,39]. This can be confirmed by the observation of a larger activation energy U of S_{asg} than that of S_{ann} in both magnetic field directions, as mentioned previously. The Zeeman fields around Fe impurities decrease and are not strong enough to delocalize triplet pairing into the bulk of the superconductor. As a result, the vortices are maintained on the surface and exhibit more 2D-like characteristics. Our results of the BKT and field-direction-dependent upper critical field $H_{c2}(\Theta)$ measurements are congruous with the above inference. The S_{ann} demonstrated 2D-like transportation behavior, while S_{asg} exhibited 3D-like transportation since there are higher Fe impurities as expected [13], which induced strong Zeeman fields and extended the zero-energy-state vortices into the bulk of S_{asg} [100]. Additionally, we also observed WAL in both samples, indicating the existence of the topological surface state. The WAL formula is typically utilized to characterize MR behavior in the low magnetic field region. In this paper, we focused the fitting on data up to ∼0.2 T. The fitting results for the S_{asg} sample are in good accord, and the S_{ann} sample aligns well at 16 K and above. However, the predicted square root behavior for the topological case is poorly matched by the data of 15.75 K and below for the S_{ann} sample, as seen in Fig. 7(d). Correspondingly, the parameter a exhibits a higher deviation for S_{ann} at temperatures <15.75 K, as shown in Fig. 7(e). Therefore, a more detailed explanation for S_{ann} is needed.

Since the S_{ann} sample exhibits a higher T_c, the MR behavior in the 15–15.75 K temperature change may exhibit mixed characteristics. When considering MR due to FF vortices driven by thermal fluctuations, the FF resistivity is expected to show a linear dependence on the applied magnetic field (the resistivity ρ_f related to the motion of vortices is $\rho_f = \frac{\Phi_0 B}{\eta c^2}$, where η represents the viscosity coefficient) [102]. However, this does not align well with the low-field MR behaviors observed at a temperature range of 15–15.75 K for S_{ann}. Consequently, the scenario of MR behavior arising from vortex movement is ruled out. The MR/ΔMC behavior of S_{ann} at low temperatures can also be attributed to a critical current issue. In the proximity of the critical temperature, the S_{ann} sample becomes superconductive, exhibiting high conductivity but with a very low critical current limit. When subjected to external magnetic fields, the small superconductive grains transition into a normal conductive state with lower conductivity. This explanation aligns with the observation that the S_{ann} sample displays a sharper superconducting transition, suggesting greater homogeneity after annealing. This effect of superconducting critical current likely contributes to the deviation from the WAL fit for S_{ann} at temperatures $<$15.75 K.

Considering that the WAL effect effectively describes the ΔMC behavior of both S_{asg} (at temperatures of 15–16 K) and S_{ann} (at temperatures of 16–17 K) in the normal-state region, the findings of this paper reasonably indicate the potential for $FeSe_{0.4}Te_{0.6}$ to exhibit a topological superconductivity state. This intriguing discovery offers a promising opportunity for further research, examining the potential influence of impurities on the properties of Fe-based topological superconductors.

V. CONCLUSIONS

In summary, we explored the exotic topological nature and superconductivity of as-grown and annealed $FeSe_{0.4}Te_{0.6}$ single crystals in terms of their unique magnetotransport properties. In their normal state, both samples exhibited a WAL effect, which can be attributed to magnetotransports dominated by topological surface states. The WAL effect gradually decreases as the sample thickness increases. Moreover, the topological surface conductivity contributed to the emergence of 2D-like superconductivity in the annealed sample; this was evidenced by a BKT transition and 2D-like vortex dynamics in mixed-state transport. The angular dependence of the upper critical field $H_{c2}(\theta)$ also demonstrated 2D-like behavior. Thus, the pinning energy as well as the Fe impurities could be reduced via the annealing process. As a result, the vortices were maintained on the surface and exhibited more 2D-like characteristics. We utilized our results to construct a phase diagram in the *H-T* plane, displaying different transport regimes arising from the vortex dynamics. Our work, demonstrating the 2D-like nature of $FeSe_{0.4}Te_{0.6}$ single crystals, supports these claims and offers a perspective on unconventional superconductors, paving the way for developing topological superconductors.

Note added. Following the conclusion of this study, recent work by Sharma *et al.* [103] has reported the observation of the topological properties of $FeSe_{0.5}Te_{0.5}$ single crystals. Their research provides evidence of MR demonstrating a nonsaturating linear behavior and a WAL effect. Furthermore, their first-principles calculations revealed the presence of a topological Dirac-semimetal cone within the electronic structure.

ACKNOWLEDGMENT

The authors thank the National Science and Technology Council of the Republic of China (Taiwan) for financial support under Grants No. MOST 111–2112-M-002–045 and No. NSTC 111–2811-M-002–150.

[1] Z. Wang, P. Zhang, G. Xu, L. K. Zeng, H. Miao, X. Xu, T. Qian, H. Weng, P. Richard, A. V. Fedorov *et al.*, Topological nature of the $FeSe_{0.5}Te_{0.5}$ superconductor, Phys. Rev. B **92**, 115119 (2015).

[2] G. Xu, B. Lian, P. Tang, X.-L. Qi, and S.-C. Zhang, Topological superconductivity on the surface of Fe-based superconductors, Phys. Rev. Lett. **117**, 047001 (2016).

[3] P. Zhang, K. Yaji, T. Hashimoto, Y. Ota, T. Kondo, K. Okazaki, Z. Wang, J. Wen, G. D. Gu, H. Ding *et al.*, Observation of topological superconductivity on the surface of an iron-based superconductor, Science **360**, 182 (2018).

[4] M. J. Gray, J. Freudenstein, S. Y. F. Zhao, R. O'Connor, S. Jenkins, N. Kumar, M. Hoek, A. Kopec, S. Huh, T. Taniguchi *et al.*, Evidence for helical hinge zero modes in an Fe-based superconductor, Nano Lett. **19**, 4890 (2019).

[5] Z. Wang, J. O. Rodriguez, L. Jiao, S. Howard, M. Graham, G. D. Gu, T. L. Hughes, D. K. Morr, and V. Madhavan, Evidence for dispersing 1D Majorana channels in an iron-based superconductor, Science **367**, 104 (2020).

[6] Y. Li, N. Zaki, V. O. Garlea, A. T. Savici, D. Fobes, Z. Xu, F. Camino, C. Petrovic, G. Gu, P. D. Johnson *et al.*, Electronic properties of the bulk and surface states of $Fe_{1+y}Te_{1-x}Se_x$, Nat. Mater. **20**, 1221 (2021).

[7] G. Li, S. Zhu, D. Wang, Y. Wang, and H.-J. Gao, Recent progress of scanning tunneling microscopy/spectroscopy study of Majorana bound states in the $FeTe_{0.55}Se_{0.45}$ superconductor, Supercond. Sci. Technol. **34**, 073001 (2021).

[8] A. Kreisel, P. J. Hirschfeld, and B. M. Andersen, On the remarkable superconductivity of FeSe and its close cousins, Symmetry **12**, 1402 (2020).

[9] T. Shibauchi, T. Hanaguri, and Y. Matsuda, Exotic superconducting states in FeSe-based materials, J. Phys. Soc. Jpn. **89**, 102002 (2020).

[10] H. Lohani, T. Hazra, A. Ribak, Y. Nitzav, H. Fu, B. Yan, M. Randeria, and A. Kanigel, Band inversion and topology of the bulk electronic structure in $FeSe_{0.45}Te_{0.55}$, Phys. Rev. B **101**, 245146 (2020).

[11] H. Hosono, A. Yamamoto, H. Hiramatsu, and Y. Ma, Recent advances in iron-based superconductors toward applications, Mater. Today **21**, 278 (2018).

[12] G. Biswal and K. Mohanta, A recent review on iron-based superconductor, Mater. Today: Proc. **35**, 207 (2021).

[13] Y. Sun, Z. Shi, and T. Tamegai, Review of annealing effects and superconductivity in $Fe_{1+y}Te_{1-x}Se_x$ superconductors, Supercond. Sci. Technol. **32**, 103001 (2019).

[14] S. Gariglio, N. Reyren, A. Caviglia, and J.-M. Triscone, Superconductivity at the $LaAlO_3/SrTiO_3$ interface, J. Phys: Condens. Matter **21**, 164213 (2009).

[15] G. Herranz, G. Singh, N. Bergeal, A. Jouan, J. Lesueur, J. Gázquez, M. Varela, M. Scigaj, N. Dix, and F. Sánchez, Engineering two-dimensional superconductivity and Rashba spin-orbit coupling in $LaAlO_3/SrTiO_3$ quantum wells by selective orbital occupancy, Nat. Commun. **6**, 6028 (2015).

[16] J. A. Bert, B. Kalisky, C. Bell, M. Kim, Y. Hikita, H. Y. Hwang, and K. A. Moler, Direct imaging of the coexistence of ferromagnetism and superconductivity at the $LaAlO_3/SrTiO_3$ interface, Nat. Phys. **7**, 767 (2011).

[17] Q. L. He, H. Liu, M. He, Y. H. Lai, H. He, G. Wang, K. T. Law, R. Lortz, J. Wang, and I. K. Sou, Two-dimensional superconductivity at the interface of a $Bi_2Te_3/FeTe$ heterostructure, Nat. Commun. **5**, 4247 (2014).

[18] B. Guo, K.-G. Shi, H.-L. Qin, L. Zhou, W.-Q. Chen, F. Ye, J.-W. Mei, H.-T. He, T.-L. Pan, and G. Wang, Evidence for topological superconductivity: Topological edge states in $Bi_2Te_3/FeTe$ heterostructure, Chin. Phys. B **29**, 097403 (2020).

[19] D. Qiu, C. Gong, S. Wang, M. Zhang, C. Yang, X. Wang, and J. Xiong, Recent advances in 2D superconductors, Adv. Mater. **33**, 2006124 (2021).

[20] C. Brun, T. Cren, and D. Roditchev, Review of 2D superconductivity: The ultimate case of epitaxial monolayers, Supercond. Sci. Technol. **30**, 013003 (2016).

[21] H. Nam, H. Chen, T. Liu, J. Kim, C. Zhang, J. Yong, T. R. Lemberger, P. A. Kratz, J. R. Kirtley, and K. Moler, Ultrathin two-dimensional superconductivity with strong spin–orbit coupling, Proc. Natl. Acad. Sci. USA **113**, 10513 (2016).

[22] T. Ito, Y. Fudamoto, A. Fukaya, I. Gat-Malureanu, M. Larkin, P. Russo, A. Savici, Y. Uemura, K. Groves, and R. Breslow, Two-dimensional nature of superconductivity in the intercalated layered systems Li_xHfNCl and Li_xZrNCl: Muon spin relaxation and magnetization measurements, Phys. Rev. B **69**, 134522 (2004).

[23] L. Wang, Y. Shi, M. Liu, A. Zhang, Y.-L. Hong, R. Li, Q. Gao, M. Chen, W. Ren, and H.-M. Cheng, Intercalated architecture of MA_2Z_4 family layered van der Waals materials with emerging topological, magnetic and superconducting properties, Nat. Commun. **12**, 2361 (2021).

[24] Z. Zhang, J.-Y. You, B. Gu, and G. Su, Emergent topological superconductivity in Bi-intercalated van der Waals layered $SiTe_2$, Phys. Rev. B **106**, 174519 (2022).

[25] T. Wang, A. Yu, Y. Mao, Y. Fang, Y. Liu, H. Zhang, W. Guo, W. Li, W. Peng, Z. Di *et al.*, The interplay between anomalous metallic and superconducting states tuned by disorder in thin flakes of kagome metal KV_3Sb_5, Supercond. Sci. Technol. **36**, 125015 (2023).

[26] H. Lian, Y. Wu, H. Xing, S. Wang, and Y. Liu, Effect of stoichiometry on the superconducting transition temperature in single crystalline $2H$-NbS_2, Phys. C: Supercond **538**, 27 (2017).

[27] D. Shen, C. N. Kuo, T. W. Yang, I. N. Chen, C. S. Lue, and L. M. Wang, Two-dimensional superconductivity and magnetotransport from topological surface states in $AuSn_4$ semimetal, Commun. Mater. **1**, 56 (2020).

[28] W.-H. Jiao, X.-F. Xu, H. Jiang, Z.-A. Xu, Q.-H. Chen, and G.-H. Cao, Possible evidence for Berezinskii-Kosterlitz-Thouless transition in Ba $(Fe_{0.91}4Co_{0.086})_2As_2$ crystals, Materials **14**, 6294 (2021).

[29] H. M. Cole, M. B. Venuti, B. Gorman, E. D. Bauer, M. K. Chan, and S. Eley, Plastic vortex creep and dimensional crossovers in the highly anisotropic superconductor $HgBa_2CuO_{4+x}$, Phys. Rev. B **107**, 104509 (2023).

[30] W. Wang, S. Kim, M. Liu, F. Cevallos, R. Cava, and N. Ong, Evidence for an edge supercurrent in the Weyl superconductor $MoTe_2$, Science **368**, 534 (2020).

[31] A. Kononov, M. Endres, G. Abulizi, K. Qu, J. Yan, D. G. Mandrus, K. Watanabe, T. Taniguchi, and C. Schönenberger, Superconductivity in type-II Weyl-semimetal WTe_2 induced by a normal metal contact, J. Appl. Phys. **129**, 113903 (2021).

[32] A. Jahin, A. Tiwari, and Y. Wang, Higher-order topological superconductors from Weyl semimetals, SciPost Phys. **12**, 053 (2022).

[33] H. Zheng and J.-F. Jia, Topological superconductivity in a $Bi_2Te_3/NbSe_2$ heterostructure: A review, Chin. Phys. B **28**, 067403 (2019).

[34] C. Huang, B. T. Zhou, H. Zhang, B. Yang, R. Liu, H. Wang, Y. Wan, K. Huang, Z. Liao, and E. Zhang, Proximity-induced surface superconductivity in Dirac semimetal Cd_3As_2, Nat. Commun. **10**, 2217 (2019).

[35] V. S. Stolyarov, S. Pons, S. Vlaic, S. V. Remizov, D. S. Shapiro, C. Brun, S. I. Bozhko, T. Cren, T. V. Menshchikova, and E. V. Chulkov, Superconducting long-range proximity effect through the atomically flat interface of a Bi_2Te_3 topological insulator, J. Phys. Chem **12**, 9068 (2021).

[36] Y. Sun, T. Yamada, S. Pyon, and T. Tamegai, Influence of interstitial Fe to the phase diagram of $Fe_{1+y}Te_{1-x}Se_x$ single crystals, Sci. Rep. **6**, 32290 (2016).

[37] K. Terao, T. Kashiwagi, T. Shizu, R. A. Klemm, and K. Kadowaki, Superconducting and tetragonal-to-orthorhombic transitions in single crystals of $FeSe_{1-x}Te_x$ $(0 \leqslant x \leqslant 0.61)$, Phys. Rev. B **100**, 224516 (2019).

[38] R. Kumar and G. D. Varma, Study of structural and magneto-transport properties of Fe (Te, Se) single crystals, Phys. Status Solidi B **257**, 1900552 (2020).

[39] Y. Sun, T. Taen, Y. Tsuchiya, Z. X. Shi, and T. Tamegai, Effects of annealing, acid and alcoholic beverages on $Fe_{1+y}Te_{0.6}Se_{0.4}$, Supercond. Sci. Technol. **26**, 015015 (2013).

[40] B. C. Sales, A. S. Sefat, M. A. McGuire, R. Y. Jin, D. Mandrus, and Y. Mozharivskyj, Bulk superconductivity at 14 K in single crystals of $Fe_{1+y}Te_xSe_{1-x}$, Phys. Rev. B **79**, 094521 (2009).

[41] D. Y. Yan, M. Yang, C. X. Wang, P. B. Song, C. J. Yi, and Y. G. Shi, Superconductivity in centrosymmetric topological superconductor candidate TaC, Supercond. Sci. Technol. **34**, 035025 (2021).

[42] Y. Liu, Y. Lin, J. Qin, Z. Wen, S. He, and Y. Zhao, Significant enhancement in J_c and suppression of J_c anisotropy for Sn-doped $FeSe_{0.4}Te_{0.6}$ single crystals, Mater. Today Commun. **31**, 103433 (2022).

[43] F. Nabeshima, Y. Kobayashi, Y. Imai, I. Tsukada, and A. Maeda, Effect of Co impurities on superconductivity of $FeSe_{0.4}Te_{0.6}$ single crystals, Jpn. J. Appl. Phys. **51**, 010102 (2011).

[44] T. Okada, F. Nabeshima, H. Takahashi, Y. Imai, and A. Maeda, Exceptional suppression of flux-flow resistivity in $FeSe_{0.4}Te_{0.6}$ by back-flow from excess Fe atoms and Se/Te substitutions, Phys. Rev. B **91**, 054510 (2015).

[45] M. Abdel-Hafiez, J. Ge, A. Vasiliev, D. Chareev, J. Van de Vondel, V. Moshchalkov, and A. Silhanek, Temperature dependence of lower critical field $H_{c1}(T)$ shows nodeless superconductivity in FeSe, Phys. Rev. B **88**, 174512 (2013).
[46] A. Carrington and F. Manzano, Magnetic penetration depth of MgB_2, Physica C **385**, 205 (2003).
[47] H. Takahashi, Y. Imai, S. Komiya, I. Tsukada, and A. Maeda, Anomalous temperature dependence of the superfluid density caused by a dirty-to-clean crossover in superconducting $FeSe_{0.4}Te_{0.6}$ single crystals, Phys. Rev. B **84**, 132503 (2011).
[48] U. R. Singh, S. C. White, S. Schmaus, V. Tsurkan, A. Loidl, J. Deisenhofer, and P. Wahl, Spatial inhomogeneity of the superconducting gap and order parameter in $FeSe_{0.4}Te_{0.6}$, Phys. Rev. B **88**, 155124 (2013).
[49] T. Konno, T. Adachi, M. Imaizumi, T. Noji, T. Kawamata, and Y. Koike, Superconducting gap and symmetry in $FeSe_{1-x}Te_x$ studied by specific heat in magnetic fields, J. Phys. Soc. Jpn. **83**, 094721 (2014).
[50] C. Uher, J. L. Cohn, and I. K. Schuller, Upper critical field in anisotropic superconductors, Phys. Rev. B **34**, 4906 (1986).
[51] T. Klein, D. Braithwaite, A. Demuer, W. Knafo, G. Lapertot, C. Marcenat, P. Rodière, I. Sheikin, P. Strobel, A. Sulpice *et al.*, Thermodynamic phase diagram of $FeSe_{0.5}Te_{0.5}$ single crystals in fields up to 28 Tesla, Phys. Rev. B **82**, 184506 (2010).
[52] J. C. Zhuang, Z. Li, X. Xu, L. Wang, W. K. Yeoh, X. Z. Xing, Z. X. Shi, X. L. Wang, Y. Du, and S. X. Dou, Pauli-limited effect in the magnetic phase diagram of $FeSe_xTe_{1-x}$ thin films, Appl. Phys. Lett. **107**, 222601 (2015).
[53] M. Shahbazi, X. L. Wang, S. R. Ghorbani, S. X. Dou, and C. T. Lin, Thermally activated flux flow in $Fe_{1.06}Te_{0.6}Se_{0.4}$ single crystal, Phys. C: Supercond **519**, 60 (2015).
[54] S. Khim, J. W. Kim, E. S. Choi, Y. Bang, M. Nohara, H. Takagi, and K. H. Kim, Evidence for dominant Pauli paramagnetic effect in the upper critical field of single-crystalline $FeTe_{0.6}Se_{0.4}$, Phys. Rev. B **81**, 184511 (2010).
[55] Y. Pan, Y. Sun, N. Zhou, X. Yi, J. Wang, Z. Zhu, H. Mitamura, M. Tokunaga, and Z. Shi, Novel Anisotropy of Upper Critical Fields in $Fe_{1+y}Te_{0.6}Se_{0.4}$, arXiv:2305.04515.
[56] Q. Zhang, G. Li, D. Rhodes, A. Kiswandhi, T. Besara, B. Zeng, J. Sun, T. Siegrist, M. D. Johannes, and L. Balicas, Superconductivity with extremely large upper critical fields in $Nb_2Pd_{0.81}S_5$, Sci. Rep. **3**, 1446 (2013).
[57] A. Gozar, G. Logvenov, L. F. Kourkoutis, A. Bollinger, L. Giannuzzi, D. Muller, and I. Bozovic, High-temperature interface superconductivity between metallic and insulating copper oxides, Nature (London) **455**, 782 (2008).
[58] R. de Bragança, M. Croitoru, A. Shanenko, and J. A. Aguiar, Effect of material-dependent boundaries on the interference induced enhancement of the surface superconductivity temperature, J. Phys. Chem **14**, 5657 (2023).
[59] L. Zhao, X. Qiu, and B. Zhao, Surface superconducting states in mesoscopic superconductors under different boundary conditions, Mod. Phys. Lett. B **17**, 1445 (2003).
[60] N. Keller, J. Tholence, A. Huxley, and J. Flouquet, Surface superconductivity in the heavy-fermion superconductor UPt_3, Phys. Rev. B **54**, 13188 (1996).
[61] B. Lv, M. Li, J. Chen, Y. Yang, S. Wu, L. Qiao, F. Guan, H. Xing, Q. Tao, and G.-H. Cao, Type-I superconductivity in noncentrosymmetric $NbGe_2$, Phys. Rev. B **102**, 064507 (2020).
[62] L. Lyard, P. Samuely, P. Szabo, T. Klein, C. Marcenat, L. Paulius, K. Kim, C. Jung, H.-S. Lee, and B. Kang, Anisotropy of the upper critical field and critical current in single crystal MgB_2, Phys. Rev. B **66**, 180502 (2002).
[63] M. Tinkham, *Introduction to Superconductivity* (Dover Publications, Mineola, 2004).
[64] G. Blatter, V. B. Geshkenbein, and A. Larkin, From isotropic to anisotropic superconductors: A scaling approach, Phys. Rev. Lett. **68**, 875 (1992).
[65] P. W. Anderson and Y. Kim, Hard superconductivity: Theory of the motion of Abrikosov flux lines, Rev. Mod. Phys. **36**, 39 (1964).
[66] H. Lei, R. Hu, E. S. Choi, and C. Petrovic, Thermally activated energy and flux-flow Hall effect of $Fe_{1+y}(Te_{1+x}S_x)_z$, Phys. Rev. B **82**, 134525 (2010).
[67] Z. Wu, J. Tao, X. Xu, L. Qiu, S. Yang, and Z. Wang, Anisotropic flux pinning energy in $FeSe_xTe_{1-x}$ single crystals, Phys. C: Supercond **528**, 39 (2016).
[68] H. C. Lei, K. F. Wang, R. W. Hu, H. Ryu, M. Abeykoon, E. S. Bozin, and C. Petrovic, Iron chalcogenide superconductors at high magnetic fields, Sci. Technol. Adv. Mater. **13**, 054305 (2012).
[69] M. Feigel'Man, V. Geshkenbein, A. Larkin, and V. Vinokur, Theory of collective flux creep, Phys. Rev. Lett. **63**, 2303 (1989).
[70] R. Markiewicz, Flux creep in high-T_c superconductors: Melting or thermal depinning? Physica C **171**, 479 (1990).
[71] A. Tsen, B. Hunt, Y. Kim, Z. Yuan, S. Jia, R. Cava, J. Hone, P. Kim, C. Dean, and A. Pasupathy, Nature of the quantum metal in a two-dimensional crystalline superconductor, Nat. Phys. **12**, 208 (2016).
[72] Y. Saito, T. Nojima, and Y. Iwasa, Highly crystalline 2D superconductors, Nat. Rev. Mater. **2**, 16094 (2016).
[73] C. Xu, L. Wang, Z. Liu, L. Chen, J. Guo, N. Kang, X.-L. Ma, H.-M. Cheng, and W. Ren, Large-area high-quality 2D ultrathin Mo_2C superconducting crystals, Nat. Mater. **14**, 1135 (2015).
[74] Z. Wang, C.-Y. Cheon, M. Tripathi, G. M. Marega, Y. Zhao, H. G. Ji, M. Macha, A. Radenovic, and A. Kis, Superconducting 2D NbS_2 grown epitaxially by chemical vapor deposition, ACS Nano **15**, 18403 (2021).
[75] Z. Liu, C. Wang, C. Xu, M. Hao, H.-M. Cheng, W. Ren, and N. Kang, Effects of domain structures on vortex state of two-dimensional superconducting Mo_2C crystals, 2D Mater. **6**, 021005 (2019).
[76] J. M. Kosterlitz and D. J. Thouless, Ordering, metastability and phase transitions in two-dimensional systems, J. Phys. C: Solid State Phys. **6**, 1181 (1973).
[77] J. Kosterlitz, The critical properties of the two-dimensional *xy* model, J. Phys. C: Solid State Phys. **7**, 1046 (1974).
[78] V. N. Ryzhov, E. Tareyeva, Y. D. Fomin, and E. N. Tsiok, Berezinskii-Kosterlitz-Thouless transition and two-dimensional melting, Phys. Usp. **60**, 857 (2017).
[79] V. Kogan, Interaction of vortices in thin superconducting films and the Berezinskii-Kosterlitz-Thouless transition, Phys. Rev. B **75**, 064514 (2007).
[80] B. Halperin and D. R. Nelson, Resistive transition in superconducting films, J. Low Temp. Phys. **36**, 599 (1979).

[81] Y. S. Lin, S. Y. Wang, X. Zhang, Y. Feng, Y. P. Pan, H. Ru, J. J. Zhu, B. K. Xiang, K. Liu, C. L. Zheng *et al.*, Direct observation of quantum anomalous vortex in Fe(Se,Te), Phys. Rev. X **13**, 011046 (2023).

[82] H.-T. He, G. Wang, T. Zhang, I.-K. Sou, G. K. Wong, J.-N. Wang, H.-Z. Lu, S.-Q. Shen, and F.-C. Zhang, Impurity effect on weak antilocalization in the topological insulator Bi_2Te_3, Phys. Rev. Lett. **106**, 166805 (2011).

[83] H. Zhang, H. Yu, D. Bao, S. Li, C. Wang, and G. Yang, Weak localization bulk state in a topological insulator Bi_2Te_3 film, Phys. Rev. B **86**, 075102 (2012).

[84] M. Veldhorst, M. Snelder, M. Hoek, C. Molenaar, D. P. Leusink, A. A. Golubov, H. Hilgenkamp, and A. Brinkman, Magnetotransport and induced superconductivity in Bi based three-dimensional topological insulators, Phys. Status Solidi RRL **7**, 26 (2013).

[85] S. Yang, Y. Fanchiang, C. Chen, C. Tseng, Y. Liu, M. Guo, M. Hong, S. Lee, and J. Kwo, Evidence for exchange Dirac gap in magnetotransport of topological insulator–magnetic insulator heterostructures, Phys. Rev. B **100**, 045138 (2019).

[86] H.-Z. Lu and S.-Q. Shen, Weak localization and weak anti-localization in topological insulators, Spintronics VII **9167**, 91672E (2014).

[87] H.-J. Kim, K.-S. Kim, J. F. Wang, M. Sasaki, N. Satoh, A. Ohnishi, M. Kitaura, M. Yang, and L. Li, Dirac versus Weyl fermions in topological insulators: Adler-Bell-Jackiw anomaly in transport phenomena, Phys. Rev. Lett. **111**, 246603 (2013).

[88] S. Singh, R. Gopal, J. Sarkar, A. Pandey, B. G. Patel, and C. Mitra, Linear magnetoresistance and surface to bulk coupling in topological insulator thin films, J. Phys.: Condens. Matter **29**, 505601 (2017).

[89] S. Barua, M. C. Hatnean, M. R. Lees, and G. Balakrishnan, Signatures of the Kondo effect in VSe_2, Sci. Rep. **7**, 10964 (2017).

[90] L. Ghosh, M. Alam, M. Singh, S. Dixit, S. V. Kumar, A. Verma, P. Shahi, Y. Uwatoko, S. Saha, A. Tiwari *et al.*, Anharmonic phonon interactions and the Kondo effect in a $FeSe/Sb_2Te_3/FeSe$ heterostructure: A proximity effect between ferromagnetic chalcogenide and di-chalcogenide, Nanoscale **14**, 10889 (2022).

[91] L. M. Wang, H. E. Horng, and H. C. Yang, Anomalous magnetotransport in $SrRuO_3$ films: A crossover from Fermi-liquid to non-Fermi-liquid behavior, Phys. Rev. B **70**, 014433 (2004).

[92] Y. Yang, G. Tang, C. Yao, X. Yan, Y. Wang, X. Xu, Z. Mao, and H. Xing, Possible Kondo scattering and its signature in Seebeck coefficient in topological superconductor $Fe_{1+y}Te_{0.55}Se_{0.45}$, J. Magn. Magn. Mater. **564**, 170126 (2022).

[93] Z. Lin, C. Mei, L. Wei, Z. Sun, S. Wu, H. Huang, S. Zhang, C. Liu, Y. Feng, and H. Tian, Quasi-two-dimensional superconductivity in $FeSe_{0.3}Te_{0.7}$ thin films and electric-field modulation of superconducting transition, Sci. Rep. **5**, 14133 (2015).

[94] T. Otsuka, S. Hagisawa, Y. Koshika, S. Adachi, T. Usui, N. Sasaki, S. Sasaki, S. Yamaguchi, Y. Nakanishi, and M. Yoshizawa, Incoherent-coherent crossover and the pseudogap in Te-annealed superconducting $Fe_{1+y}Te_{1-x}Se_x$ revealed by magnetotransport measurements, Phys. Rev. B **99**, 184505 (2019).

[95] T. Machida, Y. Sun, S. Pyon, S. Takeda, Y. Kohsaka, T. Hanaguri, T. Sasagawa, and T. Tamegai, Zero-energy vortex bound state in the superconducting topological surface state of Fe(Se,Te), Nat. Mater. **18**, 811 (2019).

[96] H. Miao, W. H. Brito, Z. P. Yin, R. D. Zhong, G. D. Gu, P. D. Johnson, M. P. M. Dean, S. Choi, G. Kotliar, W. Ku *et al.*, Universal $2\Delta_{max}/k_BT_c$ scaling decoupled from the electronic coherence in iron-based superconductors, Phys. Rev. B **98**, 020502 (2018).

[97] A. Ghazaryan, A. Kirmani, R. M. Fernandes, and P. Ghaemi, Anomalous Shiba states in topological iron-based superconductors, Phys. Rev. B **106**, L201107 (2022).

[98] R. Song, P. Zhang, X.-T. He, and N. Hao, Ferromagnetic impurity induced Majorana zero mode in iron-based superconductors, Phys. Rev. B **106**, L180504 (2022).

[99] L. Kong, L. Cao, S. Zhu, M. Papaj, G. Dai, G. Li, P. Fan, W. Liu, F. Yang, X. Wang *et al.*, Majorana zero modes in impurity-assisted vortex of LiFeAs superconductor, Nat. Commun. **12**, 4146 (2021).

[100] A. Ghazaryan, P. L. Lopes, P. Hosur, M. J. Gilbert, and P. Ghaemi, Effect of Zeeman coupling on the Majorana vortex modes in iron-based topological superconductors, Phys. Rev. B **101**, 020504 (2020).

[101] P. Doak, G. Balduzzi, P. Laurell, E. Dagotto, and T. A. Maier, Spin-singlet topological superconductivity in the attractive Rashba-Hubbard model, Phys. Rev. B **107**, 224501 (2023).

[102] Y. Kim, C. Hempstead, and A. Strnad, Flux-flow resistance in type-II superconductors, Phys. Rev. **139**, A1163 (1965).

[103] M. Sharma, N. Karn, and V. Awana, Normal state magneto transport properties of $FeSe_{0.5}Te_{0.5}$ superconductor: The role of topological surface states, arXiv:2307.01476.